Sea State and Boundary Layer Stability Limit Sea Spray Aerosol Lifetime over the Southern Ocean

Sebastian Landwehr[1], Michele Volpi[2], Marzieh H Derkani[3], Filippo Nelli[4], Alberto Alberello[5], Alessandro Toffoli[4], Martin Gysel-Beer[6], Robin L Modini[6], and Julia Schmale[7]

[1]EPFL
[2]Swiss Data Science Center
[3]The University of The University of Melbourne
[4]The University of Melbourne
[5]University of Adelaide
[6]Paul Scherrer Institute
[7]École Polytechnique Fédérale de Lausanne

November 23, 2022

Abstract

A data set of concurrent measurements of sea spray aerosol concentration, wind speed, sea state, and air and water temperature was acquired across all sectors of the Southern Ocean during the Antarctic Circumnavigation Expedition (Austral summer 2016/2017). In addition to the established dependence on wind speed, our observations demonstrate that sea spray aerosol concentrations depend on sea state and the stability of the marine boundary layer. Besides driving sea spray emissions, wind speed and sea state strongly influence the deposition onto the ocean surface and thus aerosol lifetime even for smaller particles. Stable atmospheric conditions allow a typical lifetime of up to 4 days, while tropospheric air entrainment in unstable conditions reduces the residence time of sea spray aerosol in the marine boundary layer to less than 2 days.

Sea State and Boundary Layer Stability Limit Sea Spray Aerosol Lifetime over the Southern Ocean

S. Landwehr*[1,2], M. Volpi[3], M. H. Derkani[4], F. Nelli[4], A. Alberello[5,6], A. Toffoli[4], M. Gysel-Beer[2], R. L. Modini[2], J. Schmale*[1,2]

[1]Extreme Environments Research Laboratory, École Polytechnique Fédérale de Lausanne, School of Architecture, Civil and Environmental Engineering, Lausanne, Switzerland
[2]Paul Scherrer Institute, Laboratory of Atmospheric Chemistry, Villigen, Switzerland
[3]Swiss Data Science Center, ETH Zurich and EPFL, Switzerland
[4]Department of Infrastructure Engineering, The University of Melbourne, Parkville, Victoria 3010, Australia
[5]School of Mathematical Sciences, University of Adelaide, Adelaide, 5005, South Australia, Australia
[6]Department of Physics, Università di Torino, Turin, 10125, Italy

Key Points:

- A data set of concurrent measurements of sea spray aerosol concentration, meteorological and sea state variables over the Southern Ocean
- For 1 µm particles, dry deposition in rough seas can be enhanced by one to two orders of magnitude compared to a calm water surface
- Tropospheric air entrainment limits sea spray aerosol lifetime to 2 days in an unstable boundary layer compared to 4 days in stable conditions

Corresponding author: Sebastian Landwehr, `sebastian.landwehr@epfl.ch`

Corresponding author: Julia Schmale, `julia.schmale@epfl.ch`

Abstract

A data set of concurrent measurements of sea spray aerosol concentration, wind speed, sea state, and air and water temperature was acquired across all sectors of the Southern Ocean during the Antarctic Circumnavigation Expedition (Austral summer 2016/2017). In addition to the established dependence on wind speed, our observations demonstrate that sea spray aerosol concentrations depend on sea state and the stability of the marine boundary layer. Besides driving sea spray emissions, wind speed and sea state strongly influence the deposition onto the ocean surface and thus aerosol lifetime even for smaller particles. Stable atmospheric conditions allow a typical lifetime of up to 4 days, while tropospheric air entrainment in unstable conditions reduces the residence time of sea spray aerosol in the marine boundary layer to less than 2 days.

Plain Language Summary

We present a data set of concurrent measurements of sea spray aerosol concentration, wind speed, sea state, as well as air and water temperature, which was acquired across all sectors of the Southern Ocean during the Antarctic Circumnavigation Expedition (Austral summer 2016/2017). In addition to the established dependence on wind speed, our observations demonstrate that sea spray aerosol concentrations correlate with the sea state and depend on the stability of the marine boundary layer (the lowest layer in the atmosphere). Besides driving sea spray emissions, wind speed and sea state influence the loss of particles onto the ocean surface and thus the time that sea spray aerosols spend in the marine boundary layer. The aerosols' lifetime is further affected by atmospheric stability. When the air is colder than the water, the atmosphere is unstable and vertical mixing leads to the dilution of sea spray aerosols, which reduces their residence time in the marine boundary layer to less than two days. When the air is warmer than the water, the atmosphere is stable and weak vertical mixing allows the sea spray aerosols to accumulate in the marine boundary layer, enhancing their lifetime up to four days and consequently increasing their concentration.

1 Introduction

Sea spray aerosol particles (SSA) are hygroscopic mixtures of salts, organic matter, and water whose size changes depending on relative humidity (RH; Lewis, 2006; Zieger et al., 2017; Lewis, 2019). SSA form at the sea surface through breaking waves, via bubble bursting or wind shear on wave crests (Monahan et al., 1986; Veron, 2015). SSA provide the largest aerosol mass flux to the atmosphere (e.g. Gong et al., 2002; Seinfeld & Pandis, 2006) and affect the Earth's radiative balance and climate through directly scattering radiation (e.g. de Leeuw et al., 2011; Paulot et al., 2020) and by acting as cloud condensation nuclei (CCN) as described in Andreae and Rosenfeld (2008). Carslaw et al. (2013) estimate the global net radiative forcing (RF) of SSA to be approximately $-1.1\,\mathrm{W\,m^{-2}}$; for comparison, CO_2 exerts an RF of $+1.68(\pm0.35)\,\mathrm{W\,m^{-2}}$.

Uncertainties in aerosol properties and concentrations lead to biases in predicting RF in climate models (Trenberth & Fasullo, 2010; Flato et al., 2013). Lack of model reliability is especially exacerbated over the Southern Ocean (Myhre et al., 2013) due to notable under-estimation of cloud coverage. The issue is partly attributed to the over-prediction of ice nucleating particles in the cold sector of frontal systems (Vergara-Temprado et al., 2018), but this process alone cannot explain the full extent of the bias. Observations and modelling studies suggest that modulation of CCN by SSA concentration remains a notable source of uncertainties for cloud coverage and hence RF (Myhre et al., 2013; McCoy et al., 2015; Humphries et al., 2016; P. K. Quinn et al., 2017; Schmale, Baccarini, et al., 2019; Fossum et al., 2020).

SSA concentrations in the marine boundary layer (MBL) are controlled by emission fluxes as well as various removal and dispersion processes (Lewis & Schwartz, 2004; Zheng et al., 2018). All these processes are parameterized in climate models. Emission fluxes are historically considered to depend on wind speed (Gong, 2003). After emissions, vertical mixing induced by shear driven turbulence counteracts the particle settling, producing SSA concentrations profiles in the MBL with a weak height dependence for small particles and a stronger gradient for large particles (Clarke & Kapustin, 2002; Lewis & Schwartz, 2004). If atmospheric conditions are unstable, i.e. when the air is colder than the water, turbulence is enhanced through convection (Monin & Obukhov, 1954). Convective processes intensify the exchange across the capping inversion often present at the top of the MBL and lead to entrainment of free tropospheric, air (Stull, 1976; Wood & Bretherton, 2004). In the free troposphere air is typically depleted of SSA (Murphy et al., 2019) because they serve as CCN and are easily washed out by rain during convective events (Yu et al., 2019). Therefore the reduction of the SSA concentration in the MBL is proportional to the rate of free tropospheric air entrainment, characterized by the entrainment velocity (v_e). In stable near-surface atmospheric conditions, i.e. when the air is warmer than the water, stratification reduces the vertical mixing within the lower MBL and restrains or even inhibits the entrainment process, i.e. v_e is very small or zero. Over the global ocean, the MBL is primarily unstable throughout the year, while stable conditions occur more frequently at high latitudes ($> 45°$) during summer (Young & Donelan, 2018).

In addition to air entrainment, particles can be removed via wet and dry deposition processes. The former includes activation of SSA as CCN in clouds, if followed by washout (Wood, 2006) and, to lesser extent, scavenging by falling rain drops (Seinfeld & Pandis, 2006; Pripachkin & Budyka, 2020). These processes can be described quantitatively with a wet deposition velocity (v_w) and typically result in an SSA lifetime of a few days (Lewis & Schwartz, 2004). The deposition of aerosols at the (water) surface in dry conditions is quantified in terms of the dry deposition velocity (v_d), which depends on the gravitational settling velocity (v_s), particle size, ambient RH, and the air friction velocity (u_*) (S. A. Slinn & Slinn, 1980; T. L. Quinn & Ondov, 1998). S. A. Slinn and Slinn (1980) parameterized v_d by accounting for the different size-dependent transport efficiencies in the turbulent flux layer a few meters above the water surface and in the diffusion layer a few millimeters above the water surface. The model was further extended and refined for the effects of interception and impaction (see W. G. N. Slinn, 1982; Zhang et al., 2001; Giardina & Buffa, 2018). Williams (1982), however, suggests sea state as an important driver of dry deposition. His model predicts that, in rough seas with high whitecap fraction, v_d is almost size-independent for particle diameters between 0.01 and $\approx 3\,\mu m$ and increases with whitecap fraction.

While wind remains the primary forcing for SSA emission, recent observations suggest that emission is driven by a combined effect of wind speed and sea states (Ovadnevaite et al., 2014; Lenain & Melville, 2016; Yang et al., 2019). Nevertheless, the specific impact of sea state on emission fluxes and removal processes, and thus SSA concentrations, has remained elusive due to a lack of extensive collocated measurements.

Here, we present an unparalleled data set consisting of more than 650 hours of open ocean concomitant observations of SSA concentrations, atmospheric conditions, and sea state variables that were acquired during the Antarctic Circumnavigation Expedition (ACE). The voyage took place from December 2016 to March 2017 aboard the research vessel Akademik Tryoshnikov (Walton & Thomas, 2018; Schmale, Baccarini, et al., 2019) and covered all sectors of the Southern Ocean, including regions that were hitherto unsampled (in situ) in terms of aerosols and sea state. Observations are used to demonstrate dependencies of open ocean SSA concentrations and deposition processes on both wind speed and sea state characteristics under stable and unstable atmospheric conditions.

2 Field Observations

Observations cover a wide range of atmospheric, meteorological, and sea state conditions. Wind speed, air temperature (T_{air}) and RH were measured using an automated weather station (Landwehr, Thomas, et al., 2019). The wind speed was corrected for airflow distortion and converted into the corresponding wind speed at 10 meter height and neutral conditions ($u_{10\mathrm{N}}$; Landwehr, Thurnherr, et al., 2019). Sea surface temperature (SST) was measured with an underway system (Haumann et al., 2020). The air-sea temperature difference ($\Delta T = T_{\mathrm{air}} - \mathrm{SST}$) is used to classify the atmospheric stability of the MBL: $\Delta T < 0°C$ for unstable conditions, representing 75% of the observations; and $\Delta T > 0°C$ for stable conditions, the remaining 25% of the data.

Aerosol number size distributions sampled at a height of approximately 15 m a.s.l with a Global Atmosphere Watch whole air inlet (Schmale et al., 2017), were measured with a TSI 3321 Aerodynamic Particle Sizer (APS), covering the aerodynamic diameter (D_a) range from 0.7 µm to 19 µm with a time resolution of five minutes (Schmale, Baccarini, et al., 2019; Schmale, Henning, et al., 2019a). For this analysis, the size range was restricted to $D_a < 6$ µm, due to insufficient counts for larger diameters. Note that particles with $D_a > 0.7$ µm are considered to be SSA, as no coarse particles from other sources (e.g., mineral dust) were observed (Schmale, Henning, et al., 2019a). Observations contaminated by the ship's exhaust were excluded (Schmale, Henning, et al., 2019b). Air mass history was inferred using the Lagrangian analysis tool LAGRANTO (Wernli & Davies, 1997; Sprenger & Wernli, 2015; Thurnherr et al., 2019, 2020) and only observations with trajectories spending more than 24 hours over the open ocean were used. Periods where the ship was within 10 km of the coast were excluded. SSA concentrations were obtained by integrating the distribution over the size range.

A correlogram of the SSA number concentrations per size bin (see SI Figure S1) revealed two sub-populations within the coarse mode, separated approximately at $D_a \approx 3$ µm, exhibiting independent variation of concentration over time. We use the integrated number concentration $N_{1..2}$ to represent the "medium" and $N_{4..5}$ to represent the "large" SSA, where the suffixes provide the diameter ranges in µm.

Sea state conditions are represented in the form of the wave energy spectrum ($S_{wave}(f)$, with f the wave frequency) as described in (Holthuijsen, 2010). $S_{wave}(f)$ was reconstructed every five minutes using ship motion records from the Inertial Measurement Unit IMU (see Alberello et al. (2020) for the data base and Nielsen (2017) for the reconstruction methods). The following parameters were computed from the wave spectrum: significant wave height $H_s = 4\sqrt{m_0}$, where $m_0 = \int S(f)df$ is the zero-th order moment of the wave energy spectrum (i.e. the variance), mean energy period $T_{m-1,0} = m_1\, m_0^{-1}$, where $m_1 = \int f^{-1} S(f)df$, the corresponding wavelength $L_{m-1,0} = g\, T_{m-1,0}^2\, (2\pi)^{-1}$, and wave steepness ($\beta = \pi\, H_s\, L_{m-1,0}^{-1}$). The latter is a measure of the shape of the waves and is more related to whitecaps and wave breaking probability, and thus SSA emission, than H_s (Toffoli et al., 2010). Note that the sea state refers to the total sea and no distinction between wind sea and swell is accounted for.

All measurements were averaged over 20-minute intervals to remove turbulence-related variability.

3 Results and Discussion

3.1 SSA Concentration Versus Wind Speed, Sea State, and Atmospheric Stability

Figure 1 shows the relation between $N_{1..2}$ and $N_{4..5}$ with $u_{10\mathrm{N}}$ and β subdivided into stable and unstable atmospheric conditions. Under stable atmospheric conditions, $N_{1..2}$ and $N_{4..5}$ are on average larger than during unstable conditions for the same wind

speed and sea state. For $N_{1..2}$, the global average (median) of the concentrations during stable atmospheric conditions is 90% (160%) higher than during unstable conditions. For $N_{4..5}$ the difference is 60% (90%). Regardless of atmospheric stability $N_{1..2}$ and $N_{4..5}$ increase monotonically for $u_{10N} \gtrapprox 3\,\mathrm{m\,s^{-1}}$ and $\beta \gtrapprox 0.045$. Notably, for $u_{10N} \lessapprox 3\,\mathrm{m\,s^{-1}}$ and $\beta \lessapprox 0.045$, the bin-median concentrations show little or even negative trends with the forcing parameters.

Together, emission flux, removal and dilution processes determine the observed number concentrations leading to the complex relationship of the SSA number concentration with wind speed wave steepness, and atmospheric stability, shown by Figure 1. For low wind, the ocean surface is smooth (Toffoli et al., 2010) and the SSA emission flux is negligible due to the absence of wave breaking and hence changes in the SSA concentration are driven by deposition and dilution. With increasing wind speed and larger wave steepness, wave breaking probability and hence SSA emissions increase rapidly (Monahan et al., 1986). Note that growing wind speed also leads to faster vertical transport in the MBL, while the increase in wave steepness leads also to an enhanced impaction of particles at the water surface (S. A. Slinn & Slinn, 1980) and enhanced deposition over the area covered by whitecaps (Williams, 1982).

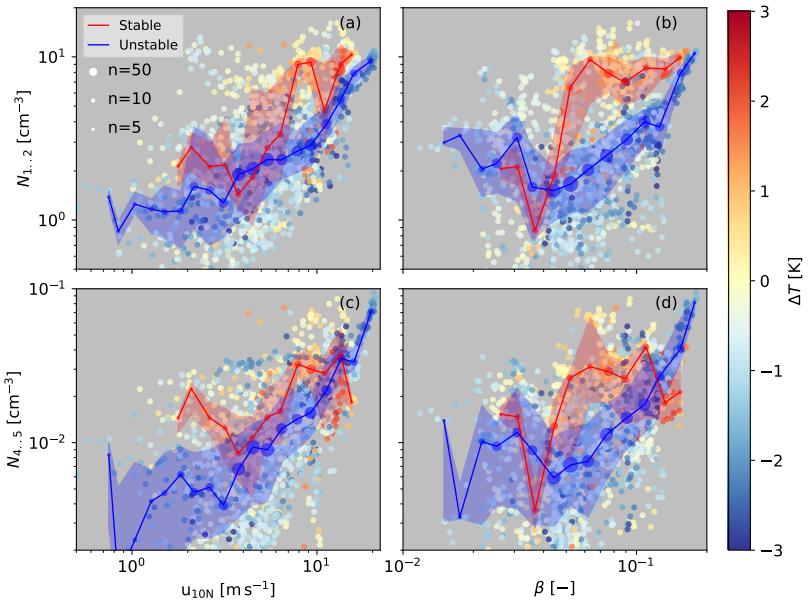

Figure 1. (a): $N_{1..2}$ as a function of u_{10N} and ΔT. The lines and shaded areas show u_{10N}-binned median and the IQR for stable and unstable atmospheric conditions, respectively. They are calculated over bins with an equal logarithmic width of log(1.3), i.e., each bin covers a 30% increase in u_{10N}. Bin-centres are placed every log(1.15), producing a 50% overlap. The marker size denotes the number of observations per bin; (b): same as (a) but for β instead of u_{10N}; (c) and (d): same as (a) and (b), respectively for $N_{4..5}$ instead of $N_{1..2}$.

3.2 The Joint Effect of Wind Speed and Sea State

Figure 2 shows the separate contributions of u_{10N} and β to sea spray aerosol concentration: the correlation with wind speed for clusters of wave steepness is presented in panels a and c, and correlation with wave steepness for different bins of wind speed is in panels b and d. Despite the obvious relation between u_{10N} and β (see SI Figure S3), the positive relation between concentration and wind speed is not conditional on wave steepness. Likewise, the dependence of concentrations on wave steepness is not constrained by wind speed and higher SSA concentrations occur for higher wave steepness at the same wind speed. These observations provide evidence that the two forcing variables have independent contributions. Interestingly, Figure 2 identifies two distinct regimes, which emerge more clearly here compared to Figure 1: (i) for $u_{10N} \lessapprox 3\,\mathrm{m\,s^{-1}}$, the median concentrations show no variation with u_{10N} (see Figure 2a and c), as wind-driven wave breaking does not occur at such low wind speeds. For $\beta \lessapprox 0.045$, on the other hand, the concentrations show a predominately negative trend with β, while the trend with u_{10N} is consistently positive (see Figure 2b and c); (ii) with increasing wind speed and wave steepness, wave breaking increases and a positive trends of the concentrations with both u_{10N} and β emerge.

To measure the individual and joint correlations of u_{10N} and β to the SSA concentration, a single (cyan dashed lines in Figure 2) and two-parameter fit (blue dashed lines) of the form

$$\log(N) = A \cdot \log(u_{10N}) + B \cdot \log(\beta) + C \tag{1}$$

are applied to the data. Only observations for $u_{10N} > 3\,\mathrm{m\,s^{-1}}$ and $\beta > 0.045$ are used to focus on the regime, where SSA concentrations are driven by emissions. The curve fitting indicates that a combination of wind speed and wave steepness explains the observations better than the single parameter fits; the coefficient of determination (R^2) is larger when using both variables than when using only one variable. Although u_{10N} and β have similar exponents (A, B) in the two parameter fits, it is worth noting that $N_{1..2}$ and $N_{4..5}$ appear to be more sensitive to u_{10N} as indicated by the higher R^2 of the single parameter fits. The fewer observations during stable atmospheric conditions preclude a more detailed analysis of the trends. However they appear to be similar to those found under unstable atmospheric conditions (see SI Figure S4).

3.3 Sea State Related Enhancement of the Dry Deposition Velocity

The SSA concentrations are a product of the local and upwind meteorological conditions that determine the emission and removal fluxes. Owing to the rapid variability of environmental conditions (in the order of hours), steady state cannot be achieved during the lifetime of SSA (in the order of days). Nevertheless, an equilibrium between emission and removal can be hypothesized if observed SSA concentrations are treated as average values over a large number of observations made under similar environmental conditions. Therefore, a balance between the size-dependent SSA emission flux (F) and the total loss rate can be expressed as:

$$\langle F \rangle = \langle N \cdot (v_d + v_e + v_w) \rangle\,, \tag{2}$$

where the angular brackets denote the expected values and $(v_d + v_e + v_w)$ is the total loss rate. Here v_w denotes the loss rate due to wet removal within the MBL. We assume v_w to be approximately constant, based on the observation that SSA concentrations showed no correlation with precipitation observed locally or predicted upwind by the ERA-5 reanalysis (see SI Text S4 and Figures S5, S6, and S7). For simplicity we assume that free tropospheric air does not contain SSA, i.e., there is complete wet removal when marine air enters the free troposphere (Yu et al., 2019).

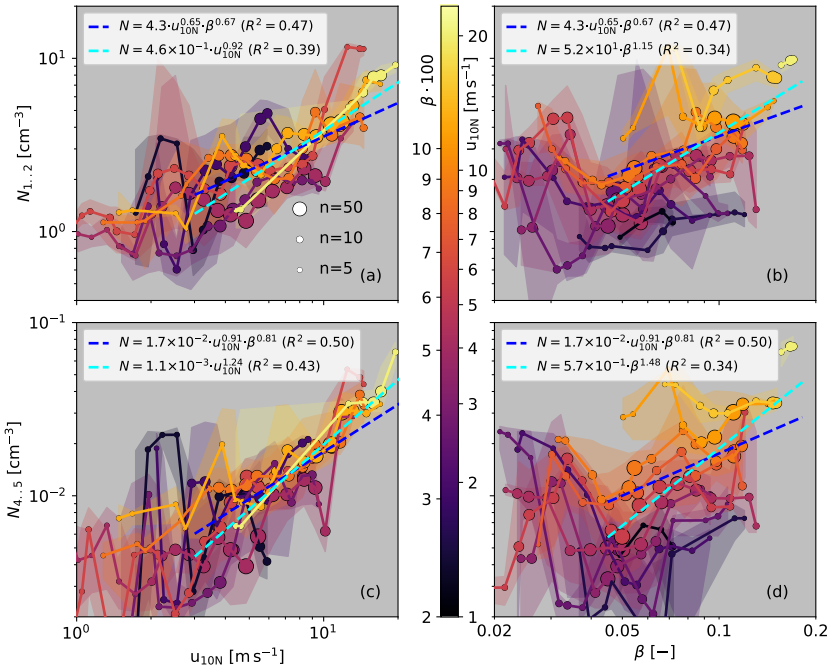

Figure 2. (a): $N_{1..2}$ as function of u_{10N} and β during unstable conditions. The lines and shaded areas show $u_{10N} \times \beta$-binned median and IQR, which are calculated over bins with an equal logarithmic with of log(1.3), i.e., each bin covers 30% increases in u_{10N} and/or β. The bins have a 50% overlap for u_{10N} and are non-overlapping for β. The line and marker colors indicate the bin-median of β and the marker size denotes the number of observations per bin; (b) same as (a) with swapped roles for β and u_{10N}; (c) and (d): same as (a) and (b), but for $N_{4..5}$; Blue and cyan lines show the result of single and two parameter fits based on equation (1) with $u_{10N} > 3\,\mathrm{m\,s^{-1}}$ and $\beta > 0.045$. The two parameter fit is displayed using a fixed u_{10N}=8 m s^{-1} ($\beta = 0.08$) and varying β (u_{10N}).

The influence of atmospheric stability on the concentration profiles, the emission flux, and the deposition velocity can be neglected, since the range of atmospheric stability observed during the expedition was limited (see Figure 1). This allows to equate the emission fluxes under stable and unstable conditions. Considering $v_{e,\mathrm{Stable}} \approx 0$ we obtain

$$\frac{\langle v_d + v_w \rangle}{\langle v_e \rangle} = \frac{\langle N_{\mathrm{Unstable}} \rangle}{\langle N_{\mathrm{Stable}} \rangle - \langle N_{\mathrm{Unstable}} \rangle}, \tag{3}$$

which relates the observed concentrations and removal processes.

Equation (3) is used to derive v_d. The steps are as follows. First, the process requires pairs of observations during stable and unstable atmospheric conditions at similar wind speed, sea state, and RH. Such pairs are selected applying a K-means clustering (Macqueen, 1967), resulting in 9 cluster pairs, with 7 to 70 observations per cluster. For each cluster pair, median concentrations ($\langle N_{\mathrm{Stable}} \rangle$ and $\langle N_{\mathrm{Unstable}} \rangle$) are calculated and the variability is measured via bootstrapping (see SI Text S6 for details). Second, because better agreement between the deposition velocity models exist at large diameters (Lewis & Schwartz, 2004), $N_{4..5}$ is used to initially estimate v_e from equation (3).

In this step v_w is neglected because it is much smaller than v_d for these diameters. Third v_e, is used to estimate v_d+v_w for the entire size range. The Williams (1982) model predicts $(v_d - v_s)$ to increase proportionally to the white cap fraction, which also scales the SSA emission flux and is related to both wind speed and sea state. Hence we separate v_d and v_w by fitting coefficients $\mathcal{A}$, $\mathcal{B}$, and $\mathcal{C}$ to

$$(v_d - v_s)_{1..2} = \mathcal{A} \cdot (\beta \cdot u_{10\mathrm{N}})^{\mathcal{B}} + \mathcal{C}, \tag{4}$$

where the offset $\mathcal{C} = 0.7(\pm 0.2)\,\mathrm{mm\,s^{-1}}$ represents v_w (cyan line in Figure 3 a), which was used to obtain an estimate of $v_d(D_a)$ alone for each cluster pair always using equation (3).

Figure 3 shows estimates of $v_d(D_a)$ from the observations as well as the predicted deposition velocities ($\hat{v}_d$) following S. A. Slinn and Slinn (1980) and ($\tilde{v}_d$) following Williams (1982) for three wind speeds: $6\,\mathrm{m\,s^{-1}}$ (black curves), $10\,\mathrm{m\,s^{-1}}$ (purple), and $12\,\mathrm{m\,s^{-1}}$ (orange). The models are in relatively good agreement for large diameters $D_a > 3\,\mu\mathrm{m}$ but deviate for smaller sizes. Note that the Williams (1982) model produces notably higher deposition velocities, for smaller particles, as it takes the contribution of white caps at higher wind speeds into account. However a stronger sea state related enhancement of $\tilde{v}_d$ would be required to match our observations.

The inset in Figure 3 demonstrates that the deposition velocity enhancement $(v_d - v_s)$ scales with the product of wind speed and wave steepness, following equation 4. This is in line with the model of Williams (1982), which suggests such an enhancement due to higher transfer rates in rough sea conditions. This result substantiates the claim that a rough sea surface significantly enhances the dry deposition velocity and thus reduces the lifetime of SSA.

3.4 Dependency of the SSA Lifetime on Atmospheric Stability

According to Lewis and Schwartz (2004), the SSA lifetime (τ) can be estimated by the ratio of the MBL height and the sum of the loss rates:

$$\tau = \frac{z_i}{(v_d + v_w + v_e)}. \tag{5}$$

We use equation (5) with the estimates of v_d, v_w, and v_e from the 9 cluster pairs. The estimates of $\tau_{1..2}$ (τ for $N_{1..2}$) range from 1 to 5 days, for stable atmospheric conditions, and from 0.5 to 1.7 days, for unstable conditions. The estimates of $\tau_{4..5}$ range from 0.7 to 1.3 days and from 0.4 to 0.9 days, for stable and unstable atmospheric conditions respectively (see Figure 4a).

Conceptually, the correlation of SSA concentrations with SSA emissions upwind should be high for the duration of their lifetime and then drop. To obtain a benchmark estimation of the lifetime of SSA particles, ERA5 reanalysis data (Hersbach et al., 2020) are used along the air mass back trajectories to calculate SSA emissions upwind based on the Gong (2003) parametrization. We correlate the in situ measured concentrations with model concentrations (N^{int}), which are derived by accumulating the upwind emissions up to an integration times (τ_{int}), i.e. assuming zero loss rates (see SI Text S7 for model description).

Figure 4b shows the Pearson correlation coefficient R as function of τ_{int}, for $N_{1..2}$ and $N_{4..5}$, respectively. For $N_{1..2}$ and unstable atmospheric conditions the correlation coefficient is highest for $\tau_{\mathrm{int}} \approx 0.4$ days and shows a second optimum at $\tau_{\mathrm{int}} \approx 1.4$ days after which the correlation drops quickly for longer integrations times. Under stable conditions for $N_{1..2}$, the highest correlations are reached between 1 and 4 days and the correlation does not decrease significantly with longer integration times. For $N_{4..5}$ the op-

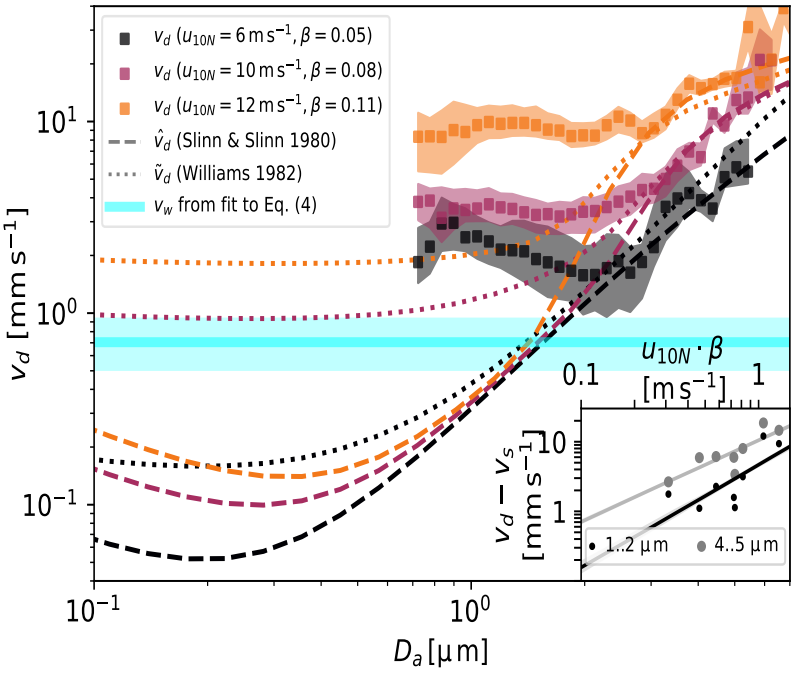

Figure 3. Deposition velocity as function of D_a: Squared markers denote the estimate of v_d using equation (3) from the clusters with a low and high value of $u_{10N} \cdot \beta$. The shaded area denotes the IQR of the bootstrap analysis. Lines and dashes show v_d based on (S. A. Slinn & Slinn, 1980) and (Williams, 1982), respectively; inset: cluster average values of $v_d - v_s$ as function $u_{10N} \cdot \beta$ for $(v_d - v_s)_{1..2}$ and $(v_d - v_s)_{4..5}$. The curves indicate the trend lines in log-space.

timal correlations are reached earlier than for $N_{1..2}$, between $\tau_{\text{int}} \approx 0.3$ days and 1 day in unstable conditions and between 1 and 2 days in stable conditions. These estimates match with the lifetimes calculated with equation (5) for each of the cluster pairs. For robustness, we repeated the exercise with the Spearman rank coefficient and obtained similar results (see SI Figure S11).

The shorter lifetime of SSA in unstable atmospheric conditions is ascribed to the entrainment of free tropospheric air at the top of the MBL, which is predominantly driven by convection. In fact, v_e estimated with equation 3 correlates strongly with $-u_* \cdot \Delta T_{\text{Unstable}}$, a tracer for the sensible heat flux at the ocean surface (see SI Figure S10). In stable conditions ($v_e = 0$) SSA lifetimes are only controlled by dry and wet deposition, which leads to a much larger variability. The effect of atmospheric stability is less pronounced for large SSA, for which the lifetime is mainly limited by dry deposition.

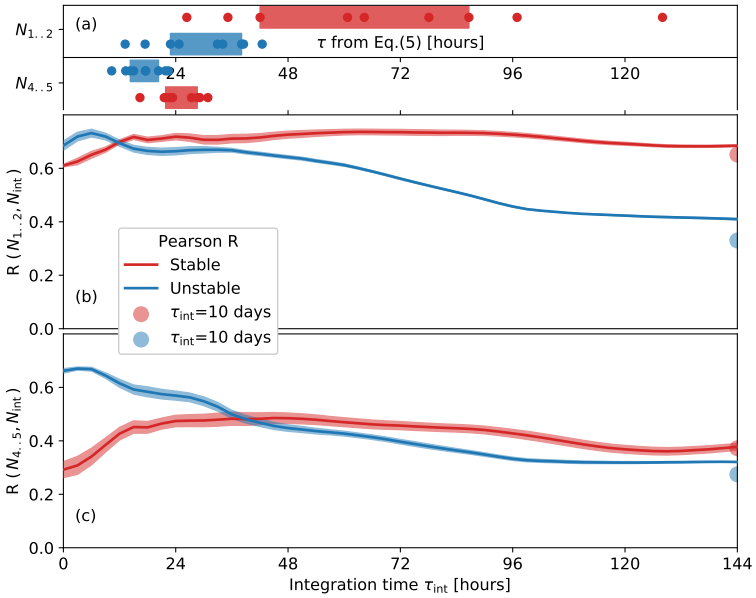

Figure 4. (a) $\tau_{1..2}$ and $\tau_{4..5}$ calculated form equation (5) for the 9 cluster pairs. The shaded squares indicate the IQR; (b) Pearson correlation coefficient between the observed number concentrations $N_{1..2}$ and $N_{\mathrm{int}}(\tau_{\mathrm{int}})$ as function of the integration time τ_{int} for stable and unstable atmospheric conditions. Correlation reached for τ_{int}=10 days is indicated by the transparent markers; (c) same as (b) but for $N_{4..5}$.

4 Conclusions

Collocated observations of wind speed, sea state, and water and air temperature (atmospheric stability) over the Southern Ocean are used to determine effects on SSA concentrations and lifetime. Results show that both wind speed and wave steepness, influence SSA number concentration through emission and deposition processes. SSA number concentration correlated positively with wind speed and wave steepness, for wind speeds $> 3\,\mathrm{m\,s^{-1}}$ and wave steepness > 0.045. For increasing wind speed and wave steepness the dry deposition velocity of particles $\lessapprox 3\,\mu\mathrm{m}$ is greatly enhanced compared to model estimates. Our analysis provides evidence that not only higher wind speed increases the dry deposition velocity, as is known, but also higher wave steepness. This aligns with the dry deposition model of Williams (1982), who suggests enhanced deposition over a water surface covered by white caps compared to an undisrupted water surface. Although our observations cover a limited size range ($0.7\,\mu\mathrm{m} < D_a < 6\,\mu\mathrm{m}$), these findings may be of high relevance for the estimation of lifetimes of smaller particles over the ocean. Results also show that atmospheric stability notably influences the SSA number concentration. During stable atmospheric conditions $N_{1..2}$ were 90% higher, and $N_{4..5}$ 60%, compared to unstable conditions. This relates to the air entrainment from the free troposphere to the MBL in unstable conditions, which dilutes the SSA concentration. We estimate an enhancement of SSA atmospheric lifetime of approximately a factor of 2 for stable conditions. Wet deposition within the MBL plays only a minor role for this dataset.

The summer Southern Ocean is characterized by a significant fraction of atmospheric stable conditions (occurring 25% of the time during the ACE voyage), a particularity of high latitudes compared to the remaining global ocean (Young & Donelan, 2018). At the same time, the region is subject to much higher wave steepness (Badulin et al., 2018). SSA is an important contribution to CCN over the Southern Ocean and hence relevant for cloud properties (Schmale, Baccarini, et al., 2019). Correctly simulating cloud cover over the Southern Ocean is important to represent the energy balance of the region and improving SSA representation in global models is likely to help reduce the bias (Regayre et al., 2020). The presented results highlight that the correct simulation of sea state together with atmospheric stability are key to estimating the lifetime and resulting climatic effects of SSA.

Acknowledgments

ACE-SPACE, JS, and AT received funding from EPFL, the Swiss Polar Institute and Ferring Pharmaceuticals. ACE-SPACE was carried out with additional support from the European FP7 project BACCHUS (grant agreement no. 49603445). SL received funding from the Swiss Data Science Center project c17-02. JS is the Ingvar Kamprad Chair of Extreme Environments, sponsored by Ferring Pharmaceuticals. AA and AT acknowledge support from the Australian Antarctic Scientific Program (AAS project 4434). AA, FN and MHD acknowledge partial support from the Cooperative Research Centres Projects, CRC-P, initiative of the Australian Government (project CRC-P53991). The data used in this study are available at `https://zenodo.org/`.

Author contributions

JS, AT, and SL conceived the study. SL designed and conducted the analyses. JS, MD, MV, FN, and AA provided quality controlled data. SL, JS and AT wrote the manuscript. All co-authors contributed to the interpretation of the data and commented on the manuscript.

References

Alberello, A., Bennetts, L., & Toffoli, A. (2020). *Antarctic Circumnavigation Expedition 2017: Motion sensor and GPS data.* Australian Antarctic Data Centre. doi: 10.4225/15/5A178EF0E5156

Andreae, M. O., & Rosenfeld, D. (2008, July). Aerosol–cloud–precipitation interactions. Part 1. The nature and sources of cloud-active aerosols. *Earth-Science Reviews*, *89*(1), 13–41. doi: 10.1016/j.earscirev.2008.03.001

Badulin, S., Grigorieva, V., Gavrikov, A., Geogjaev, V., Krinitskiy, M., & Markina, M. (2018, November). Wave steepness from satellite altimetry for wave dynamics and climate studies. *Russ. J. Earth Sci.*, *18*(5), 1–17. doi: 10.2205/2018ES000638

Carslaw, K. S., Lee, L. A., Reddington, C. L., Pringle, K. J., Rap, A., Forster, P. M., ... Pierce, J. R. (2013, November). Large contribution of natural aerosols to uncertainty in indirect forcing. *Nature*, *503*(7474), 67–71. doi: 10.1038/nature12674

Clarke, A. D., & Kapustin, V. N. (2002, February). A Pacific Aerosol Survey. Part I: A Decade of Data on Particle Production, Transport, Evolution, and Mixing in the Troposphere. *J. Atmos. Sci.*, *59*(3), 363–382. doi: 10.1175/1520-0469(2002)059⟨0363:APASPI⟩2.0.CO;2

de Leeuw, G., Andreas, E. L., Anguelova, M. D., Fairall, C. W., Lewis, E. R., O'Dowd, C., ... Schwartz, S. E. (2011, May). Production flux of sea spray aerosol. *Reviews of Geophysics*, *49*(2). doi: 10.1029/2010RG000349

Flato, G., Marotzke, J., Abiodun, B., Braconnot, P., Chou, S. C., Collins, W., ... Rummukainen, M. (2013). Evaluation of climate models. In T. F. Stocker et al. (Eds.), *Climate change 2013: The physical science basis. Contribution of working group I to the fifth assessment report of the intergovernmental panel on climate change* (pp. 741–882). Cambridge, UK: Cambridge University Press. doi: 10.1017/CBO9781107415324.020

Fossum, K. N., Ovadnevaite, J., Ceburnis, D., Preißler, J., Snider, J. R., Huang, R.-J., ... O'Dowd, C. (2020, April). Sea-spray regulates sulfate cloud droplet activation over oceans. *npj Climate and Atmospheric Science*, *3*(1), 1–6. doi: 10.1038/s41612-020-0116-2

Giardina, M., & Buffa, P. (2018, May). A new approach for modeling dry deposition velocity of particles. *Atmospheric Environment*, *180*, 11–22. doi: 10.1016/j.atmosenv.2018.02.038

Gong, S. L. (2003, December). A parameterization of sea-salt aerosol source function for sub- and super-micron particles: SEA-SALT AEROSOL PRODUCTION. *Global Biogeochemical Cycles*, *17*(4), n/a-n/a. doi: 10.1029/2003GB002079

Gong, S. L., Barrie, L. A., & Lazare, M. (2002). Canadian Aerosol Module (CAM): A size-segregated simulation of atmospheric aerosol processes for climate and air quality models 2. Global sea-salt aerosol and its budgets. *Journal of Geophysical Research: Atmospheres*, *107*(D24), AAC 13-1-AAC 13-14. doi: 10.1029/2001JD002004

Haumann, F. A., Robinson, C., Thomas, J., Hutchings, J., Pina Estany, C., Tarasenko, A., ... Leonard, K. (2020). *Physical and biogeochemical oceanography data from underway measurements with an Aqualine Ferrybox during the Antarctic Circumnavigation Expedition (ACE).* Zenodo. doi: 10.5281/zenodo.3660852

Hersbach, H., Bell, B., Berrisford, P., Hirahara, S., Horányi, A., Muñoz-Sabater, J., ... Thépaut, J.-N. (2020). The ERA5 global reanalysis. *Quarterly Journal of the Royal Meteorological Society*, *146*(730), 1999–2049. doi: 10.1002/qj.3803

Holthuijsen, L. H. (2010). *Waves in oceanic and coastal waters.* Cambridge university press.

Humphries, R. S., Klekociuk, A. R., Schofield, R., Keywood, M., Ward, J., & Wilson, S. R. (2016, February). Unexpectedly high ultrafine aerosol concentrations

above East Antarctic sea ice. *Atmospheric Chemistry and Physics*, *16*(4), 2185–2206. doi: 10.5194/acp-16-2185-2016

Landwehr, S., Thomas, J., Gorodetskaya, I., Thurnherr, I., Robinson, C., & Schmale, J. (2019, August). *Quality-checked meteorological data from the Southern Ocean collected during the Antarctic Circumnavigation Expedition from December 2016 to April 2017.* Zenodo. doi: 10.5281/zenodo.3379590

Landwehr, S., Thurnherr, I., Cassar, N., Gysel-Beer, M., & Schmale, J. (2019, October). Using global reanalysis data to quantify and correct airflow distortion bias in shipborne wind speed measurements. *Atmospheric Measurement Techniques Discussions*, 1–26. doi: 10.5194/amt-2019-366

Lenain, L., & Melville, W. K. (2016, October). Evidence of Sea-State Dependence of Aerosol Concentration in the Marine Atmospheric Boundary Layer. *J. Phys. Oceanogr.*, *47*(1), 69–84. doi: 10.1175/JPO-D-16-0058.1

Lewis, E. R. (2006, November). The effect of surface tension (Kelvin effect) on the equilibrium radius of a hygroscopic aqueous aerosol particle. *Journal of Aerosol Science*, *37*(11), 1605–1617. doi: 10.1016/j.jaerosci.2006.04.001

Lewis, E. R. (2019, February). The Dependence of Radius on Relative Humidity and Solute Mass at High Relative Humidities Up to and Including 100%. *J. Geophys. Res. Atmos.*, *124*(4), 2105–2126. doi: 10.1029/2018JD030008

Lewis, E. R., & Schwartz, S. E. (2004). *Sea salt aerosol production: Mechanisms, methods, measurements and models ; a critical review* (No. 152). Washington, DC: American Geophysical Union.

Macqueen, J. (1967). Some methods for classification and analysis of multivariate observations. In *Proceedings of the fifth Berkeley symposium on mathematical statistics and probability* (Vol. 1, pp. 281–297). Oakland, CA, USA.

McCoy, D. T., Hartmann, D. L., Zelinka, M. D., Ceppi, P., & Grosvenor, D. P. (2015). Mixed-phase cloud physics and Southern Ocean cloud feedback in climate models. *Journal of Geophysical Research: Atmospheres*, *120*(18), 9539–9554. doi: 10.1002/2015JD023603

Monahan, E. C., Spiel, D. E., & Davidson, K. L. (1986). A Model of Marine Aerosol Generation Via Whitecaps and Wave Disruption. In E. C. Monahan & G. M. Niocaill (Eds.), *Oceanic Whitecaps* (Vol. 2, pp. 167–174). Dordrecht: Springer Netherlands. doi: 10.1007/978-94-009-4668-2_16

Monin, A. S., & Obukhov, A. M. F. (1954). Basic laws of turbulent mixing in the surface layer of the atmosphere. *Contrib. Geophys. Inst. Acad. Sci. USSR*, *151*(24), 163–187.

Murphy, D. M., Froyd, K. D., Bian, H., Brock, C. A., Dibb, J. E., DiGangi, J. P., ... Yu, P. (2019, April). The distribution of sea-salt aerosol in the global troposphere. *Atmospheric Chemistry and Physics*, *19*(6), 4093–4104. doi: 10.5194/acp-19-4093-2019

Myhre, G., Shindell, D., Bréon, F.-M., Collins, W., Fuglestvedt, J., Huang, J., ... Shine, K. (2013). Anthropogenic and Natural Radiative Forcing. In *Climate change 2013: The physical science basis. Contribution of working group I to the fifth assessment report of the intergovernmental panel on climate change* (pp. 659–740). Cambridge, UK: Cambridge University Press. doi: 10.1017/CBO9781107415324.018

Nielsen, U. D. (2017). A concise account of techniques available for shipboard sea state estimation. *OCEAN ENG*, *129*, 352–362. doi: 10.1016/j.oceaneng.2016.11.035

Ovadnevaite, J., Manders, A., de Leeuw, G., Ceburnis, D., Monahan, C., Partanen, A.-I., ... O'Dowd, C. D. (2014, February). A sea spray aerosol flux parameterization encapsulating wave state. *Atmospheric Chemistry and Physics*, *14*(4), 1837–1852. doi: 10.5194/acp-14-1837-2014

Paulot, F., Paynter, D., Winton, M., Ginoux, P., Zhao, M., & Horowitz, L. W. (2020). Revisiting the impact of sea salt on climate sensitivity. *Geophysical*

Research Letters, *46*. doi: 10.1029/2019GL085601

Pripachkin, D., & Budyka, A. (2020). Influence of Aerosol Particle Parameters on Their Scavenging from the Atmosphere by Raindrops. *Izvestiya - Atmospheric and Ocean Physics*, *56*(2), 173–178. doi: 10.1134/S0001433820020103

Quinn, P. K., Coffman, D. J., Johnson, J. E., Upchurch, L. M., & Bates, T. S. (2017, August). Small fraction of marine cloud condensation nuclei made up of sea spray aerosol. *Nature Geoscience*, *10*(9), 674–679. doi: 10.1038/ngeo3003

Quinn, T. L., & Ondov, J. M. (1998, September). Influence of temporal changes in relative humidity on dry deposition velocities and fluxes of aerosol particles bearing trace elements. *Atmospheric Environment*, *32*(20), 3467–3479. doi: 10.1016/S1352-2310(98)00047-8

Regayre, L. A., Schmale, J., Johnson, J. S., Tatzelt, C., Baccarini, A., Henning, S., ... Carslaw, K. S. (2020, August). The value of remote marine aerosol measurements for constraining radiative forcing uncertainty. *Atmospheric Chemistry and Physics*, *20*(16), 10063–10072. doi: 10.5194/acp-20-10063-2020

Schmale, J., Baccarini, A., Thurnherr, I., Henning, S., Efraim, A., Regayre, L., ... Carslaw, K. S. (2019, July). Overview of the Antarctic Circumnavigation Expedition: Study of Preindustrial-like Aerosols and Their Climate Effects (ACE-SPACE). *Bull. Amer. Meteor. Soc.*, *100*(11), 2260–2283. doi: 10.1175/BAMS-D-18-0187.1

Schmale, J., Henning, S., Henzing, B., Keskinen, H., Sellegri, K., Ovadnevaite, J., ... Gysel, M. (2017, March). Collocated observations of cloud condensation nuclei, particle size distributions, and chemical composition. *Sci Data*, *4*(1), 1–27. doi: 10.1038/sdata.2017.3

Schmale, J., Henning, S., Tummon, F., Hartmann, M., Baccarini, A., Welti, A., ... Gysel-Beer, M. (2019a, June). *Coarse mode aerosol particle size distribution collected in the Southern Ocean in the austral summer of 2016/2017, during the Antarctic Circumnavigation Expedition.* Zenodo. doi: 10.5281/zenodo.2636709

Schmale, J., Henning, S., Tummon, F., Hartmann, M., Baccarini, A., Welti, A., ... Gysel-Beer, M. (2019b, June). *Sub-micron aerosol particle size distribution collected in the Southern Ocean in the austral summer of 2016/2017, during the Antarctic Circumnavigation Expedition.* Zenodo. doi: 10.5281/zenodo.2636700

Seinfeld, J. H., & Pandis, S. N. (2006). *Atmospheric Chemistry and Physics: From Air Pollution to Climate Change.* Wiley-Interscience.

Slinn, S. A., & Slinn, W. G. N. (1980, January). Predictions for particle deposition on natural waters. *Atmospheric Environment (1967)*, *14*(9), 1013–1016. doi: 10.1016/0004-6981(80)90032-3

Slinn, W. G. N. (1982, January). Predictions for particle deposition to vegetative canopies. *Atmospheric Environment (1967)*, *16*(7), 1785–1794. doi: 10.1016/0004-6981(82)90271-2

Sprenger, M., & Wernli, H. (2015, August). The LAGRANTO Lagrangian analysis tool – version 2.0. *Geoscientific Model Development*, *8*(8), 2569–2586. doi: 10.5194/gmd-8-2569-2015

Stull, R. B. (1976, July). The Energetics of Entrainment Across a Density Interface. *J. Atmos. Sci.*, *33*(7), 1260–1267. doi: 10.1175/1520-0469(1976)033⟨1260:TEOEAD⟩2.0.CO;2

Thurnherr, I., Kozachek, A., Graf, P., Weng, Y., Bolshiyanov, D., Landwehr, S., ... Aemisegger, F. (2019, September). Meridional and vertical variations of the water vapour isotopic composition in the marine boundary layer over the Atlantic and Southern Ocean. *Atmospheric Chemistry and Physics Discussions*, 1–40. doi: 10.5194/acp-2019-782

Thurnherr, I., Wernli, H., & Aemisegger, F. (2020, September). *10-day backward trajectories from ECMWF analysis data along the ship track of the Antarctic*

Circumnavigation Expedition in austral summer 2016/2017. Zenodo. doi: 10.5281/zenodo.4031705

Toffoli, A., Babanin, A., Onorato, M., & Waseda, T. (2010). Maximum steepness of oceanic waves: Field and laboratory experiments. *Geophysical Research Letters*, *37*(5). doi: 10.1029/2009GL041771

Trenberth, K. E., & Fasullo, J. T. (2010, January). Simulation of Present-Day and Twenty-First-Century Energy Budgets of the Southern Oceans. *J. Climate*, *23*(2), 440–454. doi: 10.1175/2009JCLI3152.1

Vergara-Temprado, J., Miltenberger, A. K., Furtado, K., Grosvenor, D. P., Shipway, B. J., Hill, A. A., ... Carslaw, K. S. (2018, March). Strong control of Southern Ocean cloud reflectivity by ice-nucleating particles. *PNAS*, *115*(11), 2687–2692. doi: 10.1073/pnas.1721627115

Veron, F. (2015). Ocean Spray. *Annual Review of Fluid Mechanics*, *47*(1), 507–538. doi: 10.1146/annurev-fluid-010814-014651

Walton, D. W. H., & Thomas, J. (2018, November). *Cruise Report - Antarctic Circumnavigation Expedition (ACE) 20th December 2016 - 19th March 2017* (Tech. Rep.). Zenodo. doi: 10.5281/zenodo.1443511

Wernli, B. H., & Davies, H. C. (1997). A lagrangian-based analysis of extratropical cyclones. I: The method and some applications. *Quarterly Journal of the Royal Meteorological Society*, *123*(538), 467–489. doi: 10.1002/qj.49712353811

Williams, R. M. (1982, January). A model for the dry deposition of particles to natural water surfaces. *Atmospheric Environment (1967)*, *16*(8), 1933–1938. doi: 10.1016/0004-6981(82)90464-4

Wood, R. (2006). Rate of loss of cloud droplets by coalescence in warm clouds. *Journal of Geophysical Research: Atmospheres*, *111*(D21). doi: 10.1029/2006JD007553

Wood, R., & Bretherton, C. S. (2004, September). Boundary Layer Depth, Entrainment, and Decoupling in the Cloud-Capped Subtropical and Tropical Marine Boundary Layer. *J. Climate*, *17*(18), 3576–3588. doi: 10.1175/1520-0442(2004)017⟨3576:BLDEAD⟩2.0.CO;2

Yang, M., Norris, S. J., Bell, T. G., & Brooks, I. M. (2019, September). Sea Spray Fluxes from the Southwest Coast of the United Kingdom – Dependence on Wind Speed and Wave Height. *Atmospheric Chemistry and Physics Discussions*, 1–23. doi: 10.5194/acp-2019-771

Young, I. R., & Donelan, M. A. (2018, September). On the determination of global ocean wind and wave climate from satellite observations. *Remote Sensing of Environment*, *215*, 228–241. doi: 10.1016/j.rse.2018.06.006

Yu, P., Froyd, K. D., Portmann, R. W., Toon, O. B., Freitas, S. R., Bardeen, C. G., ... Williamson, C. (2019). Efficient In-Cloud Removal of Aerosols by Deep Convection. *Geophysical Research Letters*, *46*(2), 1061–1069. doi: 10.1029/2018GL080544

Zhang, L., Gong, S., Padro, J., & Barrie, L. (2001, January). A size-segregated particle dry deposition scheme for an atmospheric aerosol module. *Atmospheric Environment*, *35*(3), 549–560. doi: 10.1016/S1352-2310(00)00326-5

Zheng, G., Wang, Y., Aiken, A. C., Gallo, F., Jensen, M. P., Kollias, P., ... Wang, J. (2018, December). Marine boundary layer aerosol in the eastern North Atlantic: Seasonal variations and key controlling processes. *Atmospheric Chemistry and Physics*, *18*(23), 17615–17635. doi: 10.5194/acp-18-17615-2018

Zieger, P., Väisänen, O., Corbin, J. C., Partridge, D. G., Bastelberger, S., Mousavi-Fard, M., ... Salter, M. E. (2017, July). Revising the hygroscopicity of inorganic sea salt particles. *Nature Communications*, *8*, 15883. doi: 10.1038/ncomms15883

Supporting Information for "Sea State and Boundary Layer Stability Limit Sea Spray Aerosol Lifetime over the Southern Ocean"

S. Landwehr*[1,2], M. Volpi[3], M. H. Derkani[4], F. Nelli[4], A. Alberello[5,6],

A. Toffoli[4], M. Gysel-Beer[2], R. L. Modini[2], J. Schmale*[1,2]

[1]Extreme Environments Research Laboratory, École Polytechnique Fédérale de Lausanne, School of Architecture, Civil and Environmental Engineering, Lausanne, Switzerland

[2]Paul Scherrer Institute, Laboratory of Atmospheric Chemistry, Villigen, Switzerland

[3]Swiss Data Science Center, ETH Zurich and EPFL, Switzerland

[4]Department of Infrastructure Engineering, The University of Melbourne, Victoria 3010 Australia

[5]School of Mathematical Sciences, University of Adelaide, Adelaide, 5005, South Australia, Australia

[6]Deparment of Physics, Università di Torino, Turin, 10125, Italy

Contents of this file

1. Text S1 to S7

2. Figures S1 to S11

Introduction

This supporting information is intended to provide additional details that may be relevant to further studies. Texts S1 provides additional details on the measurements of

the aerosol number concentrations; Text S2 motivates the classification of the observed SSA based on their size; Text S3 provides details on the settling and deposition velocity parametrizations; Text S4 elaborates on the lack of correlation found between SSA number concentrations and precipitation observed locally or predicted upwind by the ERA-5 reanalysis; Text S5 provides the relation between ERA-5 reanalysis estimates of the boundary layer height and the observed wind speed and atmospheric stability as well as the relation between wave steepness and $u_{10\mathrm{N}}$ during stable and unstable atmospheric conditions; Text S6 provides further detail on the analysis presented in Section 3.3; and Text S7 provides the details to the air mass back trajectory analysis and the inferring of the aerosol life-time from the correlation of the observed number concentration with the conditions encountered upwind.

Text S1: Details on the Aerosol Measurements and Size Conversions

The TSI 3321 Aerodynamic Particle Sizer (APS) was installed in a container on the foredeck behind a standard Global Atmosphere Watch whole air inlet, which cleared the container top by 1.5 m placing the sample height approximatly at 15 m a.s.l. The RH in the sampling line did not exceed 40% and it can be expected that efflorescence of the SSA particles has occurred before they were sized by the APS measured, which consequently measured the *dry* aerodynamic diameter of the particles. A test of the particle sizing in August 2018 showed high accuracy for $D_a \leq 1\,\mu\mathrm{m}$ and a potential overestimation of D_a by 22% for $D_a > 3\,\mu\mathrm{m}$. The number concentrations ($n(D_a) \coloneqq dN/d\log D_a\,|_{D_a}$) have been corrected for experimentally determined inlet line losses (17%) as described in Schmale et al. (2019).

The conversion of D_a into the volume equivalent dry diameter (D_{ve}) is given by:

$$D_{ve} = D_a \sqrt{\frac{\chi_c \cdot \rho_0}{\rho_{\mathrm{ss}}}}, \tag{S1}$$

where $\chi_c = 1.08$ is the shape factor for cubic particles and $\rho_{\mathrm{ss}} = 2.017\,\mathrm{kg\,m^{-3}}$ is the density of sea salt (Zieger et al., 2017). For SSA particles one obtains $D_{ve} \approx 0.7\,D_a$.

The diameter of the aerosols at ambient conditions ($D_p(\mathrm{RH})$) is given by

$$D_p(\mathrm{RH}) = D_{ve} \cdot g_e(\mathrm{RH}), \tag{S2}$$

were $g_e(\mathrm{RH})$ denotes the RH dependent hygroscopic growth factor of the particles.

Text S2: Classification into "Medium" and "Large" SSA

We define the number concentration integrated over a certain size range as

$$N_{x..y} \coloneqq \int_x^y n(D_a) d\log D_a \tag{S3}$$

and use $N_{1..2}$ (Diameter in µm) to represent the "medium" and $N_{4..5}$ to represent the "large" SSA, respectively. Our classification of the observed size range in "medium" and "large" SSA is motivated by the different relation of the two parts of the number size distribution with RH. This is also reflected in the correlation of $n(D_a)$ from the different size bins. Figure S1 shows the correlogram (pair wise correlation coefficients) of the number concentrations measured at the different APS size bins. Two distinct groups of aerosol populations are visible within the size range covered by the APS, that separate at $D_a \approx 3\,\mu\mathrm{m}$. The correlation between neighbouring size bins is higher for "medium" SSA, where removal and dilution processes are size independent. The cross correlation between the "large" SSA size bins decays quicker, as these are subject to stronger removal with

increasing particle size. For $D_a \gtrapprox 6\,\mu m$ the low concentrations approach the detection limit of the APS, which results in a very low correlation of neighbouring bins. For the size bins with $D_a < 1\,\mu m$ number concentrations are also less correlated, which may indicate that these number concentrations may have been influenced by other processes potentially unrelated to SSA.

Text S3: Settling and Deposition Velocity Parametrizations

The settling velocity that describes the slow falling of the particles depends on the density (ρ_p) and cross section ($\propto D_p^2$) of the particle and is given by

$$v_s = g \cdot (\rho_p - \rho_{\text{air}}) \cdot D_p^2 \cdot C_c \cdot (18\,\mu_a)^{-1}, \tag{S4}$$

were g is the constant of gravity, C_c is the Cunningham slip correction factor, ρ_{air} the density of air, and μ_a the dynamic viscosity of air.

The density and diameter of the SSA are both dependent on RH. Here we utilize the parametrisation of $g_e(\text{RH})$ for inorganic sea salt particles provided by (Lewis, 2006). Our data set covers the range $60\% < \text{RH} < 100\%$ and we make the assumption that the SSA have not undergone efflorescence during their life-time. We further neglect the size dependence of $g_e(\text{RH})$ based on the Kelvin effect (e.g., Lewis, 2006), which would suggest about 3% higher $g_e(\text{RH})$ for the observed size range. In order to account for the change in ρ_p we assume additivity of the volumina, compare Eq. (3) in (Quinn & Ondov, 1998), i.e.,

$$\rho_p(RH) = \rho_{\text{ss}} \left[g_e(\text{RH})\right]^{-3} + \rho_{\text{H}_2\text{O}} \left(1 - \left[g_e(\text{RH})\right]^{-3}\right) \tag{S5}$$

Inserting Eqations (S2) and (S5) in (S4) and neglecting the density of air, we obtain

$$v_s(\mathrm{RH}) = v_{s0}\left(g_e^2\frac{\rho_{\mathrm{H_2O}}}{\rho_{\mathrm{ss}}} + \frac{1}{g_e}(1-\frac{\rho_{\mathrm{H_2O}}}{\rho_{\mathrm{ss}}})\right), \tag{S6}$$

where v_{s0} denotes the settling velocity of dry SSA particles. For this data set, the uncertainty of D_a for larger diameters (22%) leads to a relative uncertainty in v_s of about 44%.

Text S4: No Correlation with Precipitation

During ACE precipitation $> 10^{-3}\,\mathrm{mm\,hr^{-1}}$ was observed for less than 20% of the time. During unstable atmospheric conditions weak precipitation events $< 10^{-1}\,\mathrm{mm\,hr^{-1}}$ where about two times more frequent than during stable atmospheric conditions. However, strong precipitation occurred at approximately the same frequency under both conditions (See Figure S5).

The efficiency of below-cloud scavenging has been found to be strongly dependent on aerosol size (Pripachkin & Budyka, 2020), however negligible compared to the in-cloud scavenging (Seinfeld & Pandis, 2006), which is assumed to be rather independent of size once the aerosols are large enough to act as CCN (Wood, 2006). The wet deposition velocity (within the MBL) is given by:

$$v_w = \lambda_i\, h_{\mathrm{cloud}} + \lambda_b\,(z_i - h_{\mathrm{cb}}) \approx \lambda_i\, h_{\mathrm{cb}}, \tag{S7}$$

where h_{cb} is the cloud base height, and λ_i and λ_b are the in and below cloud scavenging coefficients, which are both a function of rain rate, however λ_i depends additionally on the nucleation efficiency and λ_b on the size dependent scavenging efficiency. Albeit modulated by nucleation efficiency, wet removal scales with the precipitation rate and one would expect a negative correlation of the SSA number concentrations with precipitation. During

ACE a correlation with precipitation was not observed neither for local precipitation rates (Figure S6 a) nor for precipitation values from the ERA-5 reanalysis (Figure S6 b), also not if they were integrated along the air mass back trajectories for 12 or 24 hours (Figure S7 a, and b). This leads us to the conclusion that wet deposition within the MBL did not modulate the observed SSA concentration significantly and that we can incorporate wet deposition in Eq. (1) as an unknown constant term for which we assume: (i) $v_{w,\mathrm{Stable}} \approx v_{w,\mathrm{Unstable}}$ based on the similar distributions of the rain rate over the two subsets of stable and unstable atmospheric conditions (See Figure S5), (ii) v_w is independent of particle size within the observed size range, and (iii) $v_w \ll v_d$ for ($D_a > 4\,\mu\mathrm{m}$). Note that the efficient wet removal occurring in convective up-drafts (Yu et al., 2019) does not contribute to v_w because the thereby depleted air will predominantly leave the MBL.

Text S5: Relation of Boundary Layer Height and Wave Steepness to Wind Speed and Atmospheric Stability

The ECMWF reanalysis product ERA-5 (Hersbach et al., 2020) provides estimates of z_i based on the Richardson number method. Figure S2 shows z_i as a function of $u_{10\mathrm{N}}$ and ΔT. The data shows a strong correlation between z_i and $u_{10\mathrm{N}}$ with similar median values for stable and unstable atmospheric conditions.

Figure S3 shows β as a function of $u_{10\mathrm{N}}$ and ΔT. The data shows a strong correlation between β and $u_{10\mathrm{N}}$ with similar median values for stable and unstable atmospheric conditions.

Text S6: Details on the Number Concentration Ratio Analysis for the Estimation of Entrainment and Deposition Velocities

In order to ensure similar emission flux and dry deposition velocities, the analysis presented in Sec. 3.3 requires pairs of observations made at similar wind speed, sea state, and RH, but under stable and unstable atmospheric conditions. To obtain such pairs a k-means cluster analysis on the parameter space $\mathbf{X} = [\log(u_{10\mathrm{N}}), \log(\beta), \log(v_s(\mathrm{RH}))]$ was performed on the subset with $\Delta T > 0°C$ in order to obtain groups of data with similar conditions. For each cluster center observations with $(d < \log(1.3))$ where attributed to the cluster. This leads to a small overlap between neighbouring clusters. Corresponding observations under unstable atmospheric conditions were selected based on the euclidean distance to the cluster centres of the stable subset $(d = |\mathbf{X}_{\mathrm{Unstable}} - \mathbf{X}_{\mathbf{c},\mathrm{Stable}}|)$, requiring $(d < \log(1.3))$. From the unstable subset only observations with $\Delta T < -0.2°C$ were used, in order to ensure $v_e > 0$. The resolution of APS is $n_{min} = 3.9 \cdot 10^{-3}$ counts per size bin. In order to reduce the uncertainty due to counting statistics only observations with $n(D_a) > 4 \cdot 10^{-2}$ for $D_a \leq 5\,\mu\mathrm{m}$, where used.

The analysis was started with 25 cluster seeds, of which 16 could not be used due to insufficient number of observations in clusters for either stable or unstable atmospheric conditions. Consequently nine cluster pairs remained with observations per cluster ranging from 7 to 70 for both stable and unstable atmospheric conditions. The $[\log(u_{10\mathrm{N}}), \log(\beta)]$ coordinates of the cluster centres span a subset of the parameter space covered during ACE (Figure S8 a), since extreme values were not sampled often enough. For intermediate conditions, however, similar parameter combinations were sampled several times (Figure S8 b), so that the average of concentrations can be assumed to be similar to the steady state value.

The ratio $N_{\text{Unstable}}(N_{\text{Stable}} - N_{\text{Unstable}})^{-1}$ was calculated for each cluster pair and used to estimate v_e and then $v_d(D_a) + v_w$ (see Figure S9). The uncertainty of the estimates was inferred by running 50 bootstrap samples with 66% of the observations randomly selected from the stable and unstable cluster. The median of the bootstrap samples is used as best estimate and the IQR to infer the uncertainty. After this first iteration v_w was inferred form a fit to Eq. (4) (see inset in Figure S9).

The cluster median estimates of v_e show a strong correlation with the magnitude of the air sea temperature gradient during unstable conditions ($-\Delta T_{\text{Unstable}}$) ($R^2 = 0.74$) and wind speed ($R^2 = 0.92$), but the strongest correlation ($R^2 = 0.97$) to the product $-\Delta T_{\text{Unstable}} \cdot u_*$ that defines the sensible heat flux during unstable conditions (see Figure S10).

Text S7: Air Mass Back Trajectory Analysis

Air mass history was inferred using the Lagrangian analysis tool LAGRANTO (Wernli & Davies, 1997; Sprenger & Wernli, 2015; Thurnherr et al., 2019). Trajectories where released at various pressure levels and all back trajectories with release height $h < z_i$ were used to estimate the mean travel time over the open ocean and the time when the air masses had last been in contact with land (when they have passed a grid cell where the ERA-5 land sea mask (LSM) was non zero).

Back trajectories with release height $h < z_i$ were also used to calculate an estimated SSA concentrations base on a simplified source flux and deposition assumption: For each time step $\Delta t = 3\,\text{h}$ along the trajectory an incremental contribution to the concentration was estimated as

$$\delta N = \frac{F\,\Delta t}{z_i}\,(1 - \mathrm{LSM}), \tag{S8}$$

where the source flux F is parametrised as $F = u_{10\mathrm{N}}^{3.41}$ (Gong, 2003) and the dilution in the local boundary layer is scaled with the term z_i^{-1}, based on the assumption of efficient mixing within the MBL. The ERA-5 land sea mask (LSM) is used to restrict SSA production to the water surface. The predicted concentration is now calculated, for each back trajectory, by summing up all contributions along the trajectory up to an integration time τ_{int} and averaged over all trajectories:

$$N_{\mathrm{int}}(\tau_{\mathrm{int}}) = \left\langle \sum_{j=0}^{j=\tau_{\mathrm{int}}(\Delta t)^{-1}} \delta N_j \prod_{k=0}^{j} \sigma_k \right\rangle, \tag{S9}$$

were the source sensitivity factor (σ) is set to one as long as the trajectory remains within the boundary layer ($(h < z_i)_{t=t_j}$) and to zero once the boundary layer has been left, assuming that air masses outside of the MBL are depleted in $> 0.7\,\mu\mathrm{m}$ particles. In other words the deposition velocities are neglected.

By computing the correlation between the measured ($N_{1..2}$ and $N_{4..5}$) and $N_{\mathrm{int}}(\tau_{\mathrm{int}})$ we can achieve a rough approximation of the average life time of the SSA. Figure 4 shows the Pearson correlation coefficient of $N_{1..2}(N_{4..5})$ and $N_{\mathrm{int}}(\tau_{\mathrm{int}})$ as function of τ_{int} while Figure S11 show the Spearman rank coefficient.

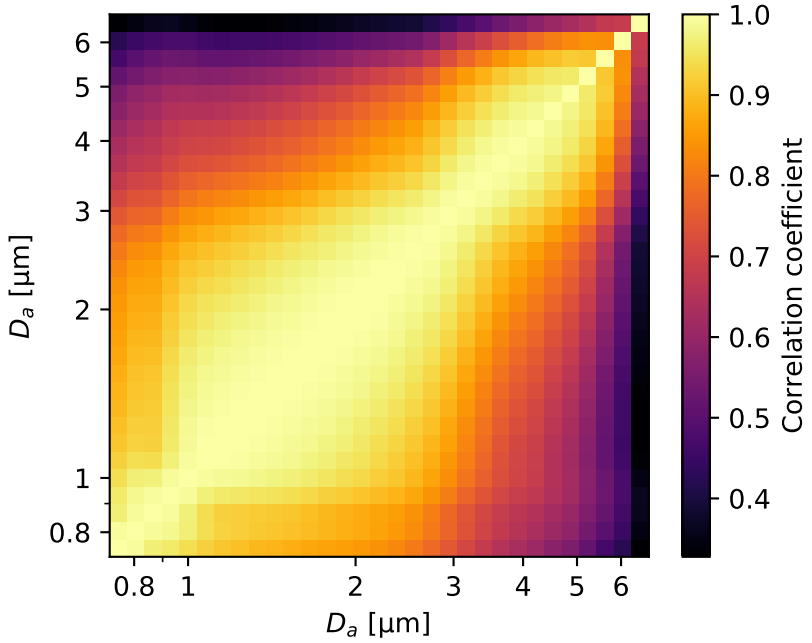

Figure S1. Correlogram of the number concentrations per size bin (correlation coefficients of the pairwise correlations).

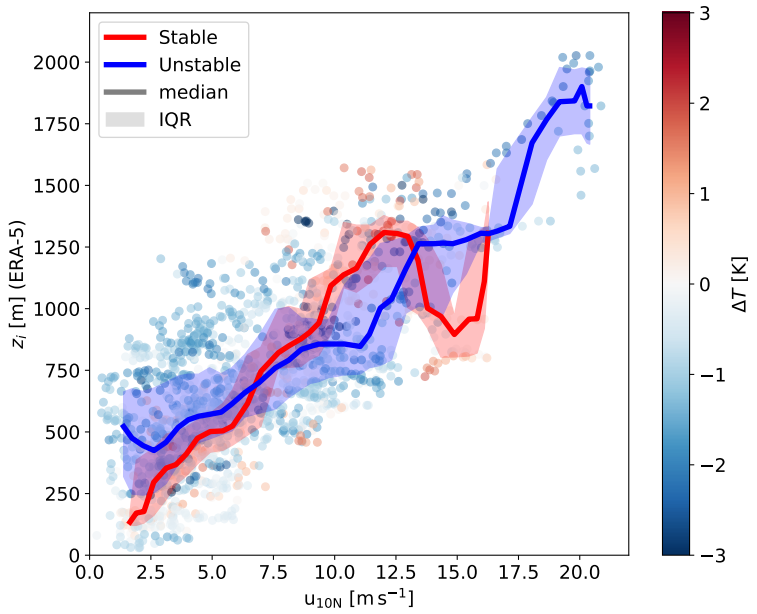

Figure S2. Boundary layer height predicted by the ERA-5 reanalysis as a function of wind speed and air-sea temperature gradient. Bin-median values and IQR, calculated over 2 m s^{-1} wide wind speed bins with 75% overlap are shown separately for stable and unstable conditions. Only data points, for which aerosol and sea state measurements where available, are shown in this figure.

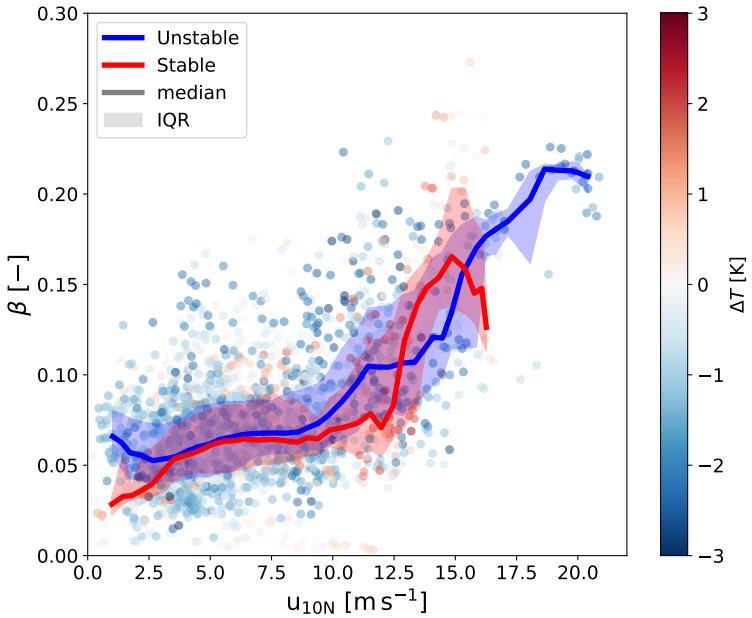

Figure S3. Wave steepness as a function of wind speed and air-sea temperature gradient. Bin-median values and IQR, calculated over $2\,\mathrm{m\,s^{-1}}$ wide wind speed bins with 75% overlap, are shown separately for stable and unstable conditions.

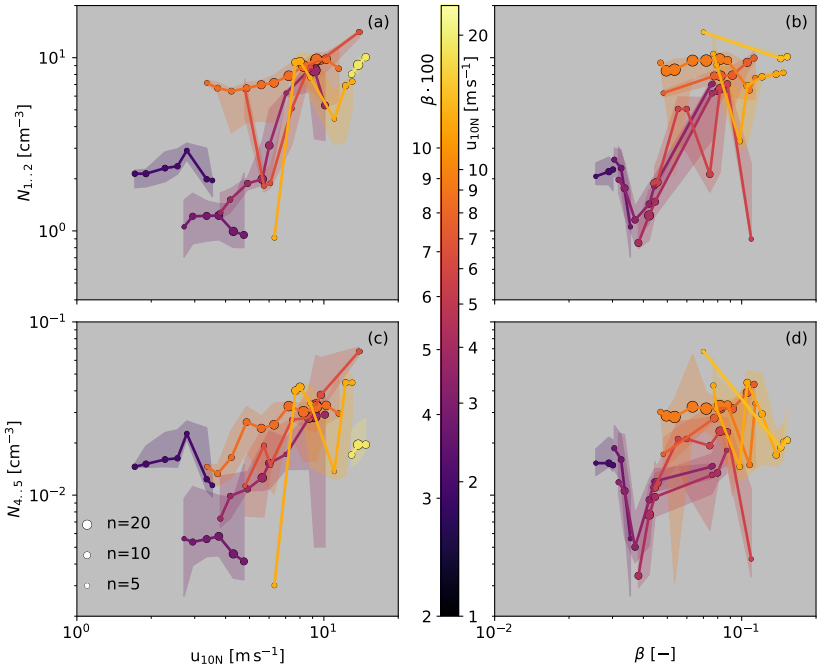

Figure S4. Pendant to Figure 2 but for stable atmospheric conditions.

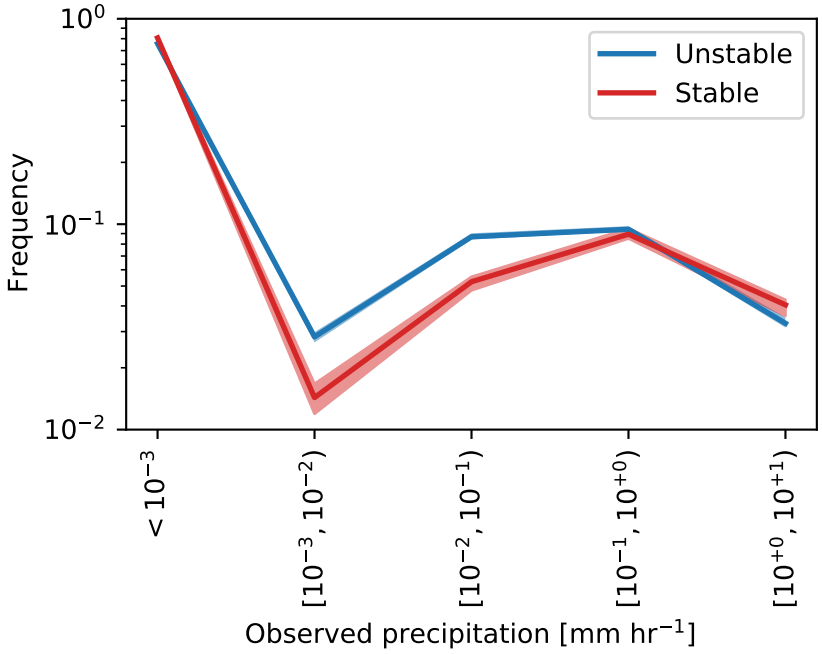

Figure S5. Histogram of total precipitation rate (rain and snow fall) observed under stable and unstable atmospheric conditions. The shading indicates the IQR estimated with a bootstrap analysis (100 runs with 66% sample size).

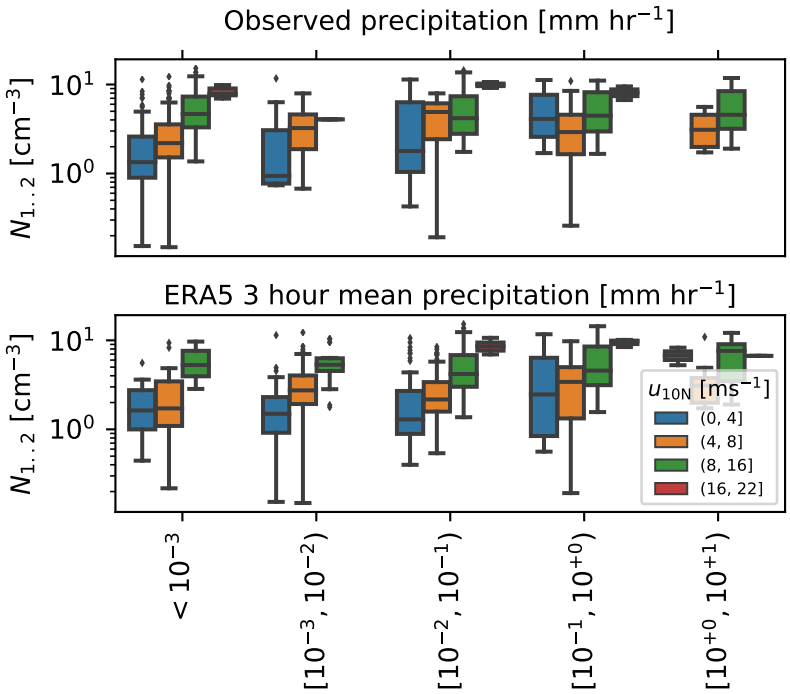

Figure S6. (a) Box and whiskers plot of $N_{1..2}$ for ranges of wind speed and observed total precipitation rate (rain and snow fall); (b) same as (a) but for total precipitation from the ERA-5 reanalysis.

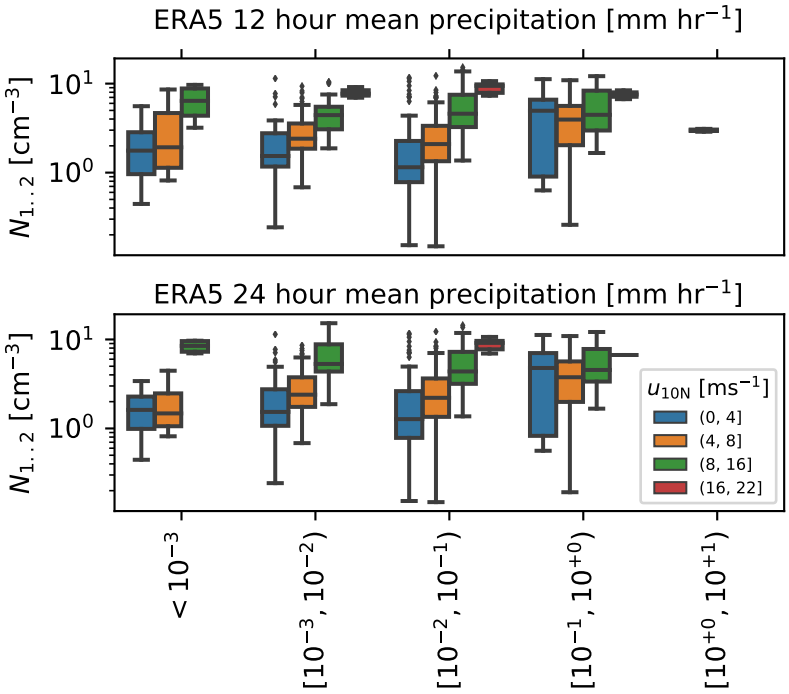

Figure S7. (a) Box and whiskers plot of $N_{1..2}$ for ranges of wind speed and ERA-5 total precipitation rate (rain and snow fall) averaged along the airmass back trajectories over the previous 12 hours; (b) same as (a) but for averaging over the previous 24 hours;

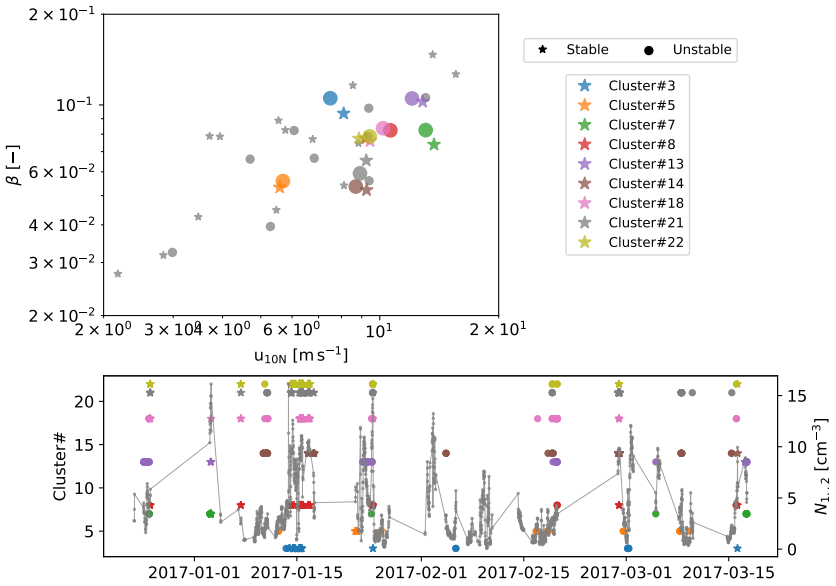

Figure S8. (a) Cluster centres as $[\log(u_{10\mathrm{N}}), \log(\beta)]$ coordinates, symbols denote stable and unstable atmospheric condition. Only the 9 clusters, which are used in the analysis are shown in color, the other cluster centres are shown in gray; (b) Centres of the used clusters (left axis) and $N_{1..2}$ (right axis) plotted as function of time.

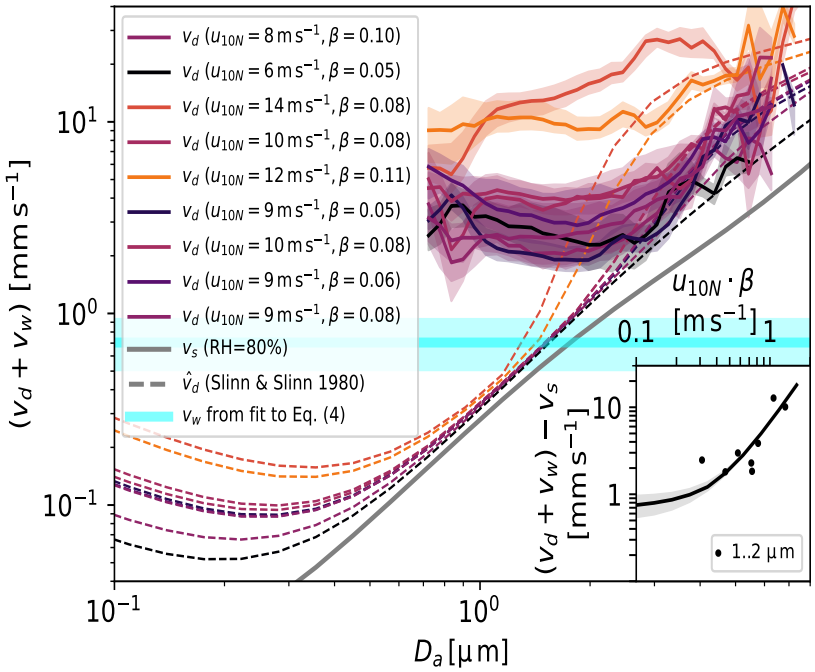

Figure S9. (a) Deposition velocities as function of D_a: the solid lines denote $(v_d(D_a) + v_w)$ estimated from each cluster pair via Eq. (4) (first iteration), with the color indicating $u_{10N} \cdot \beta$ and the shading the IQR from the bootstrap analysis. Dashed lines in matching color show $\hat{v_d}$ based on (Slinn & Slinn, 1980). The cyan line indicates the offset from the fit to Eq. (4), which we equate to v_w; (b): the scatter shows $(v_d(D_a) + v_w)_{1..2}$ as function of $u_{10N} \cdot \beta$ and the line the best fit to Eq. (4).

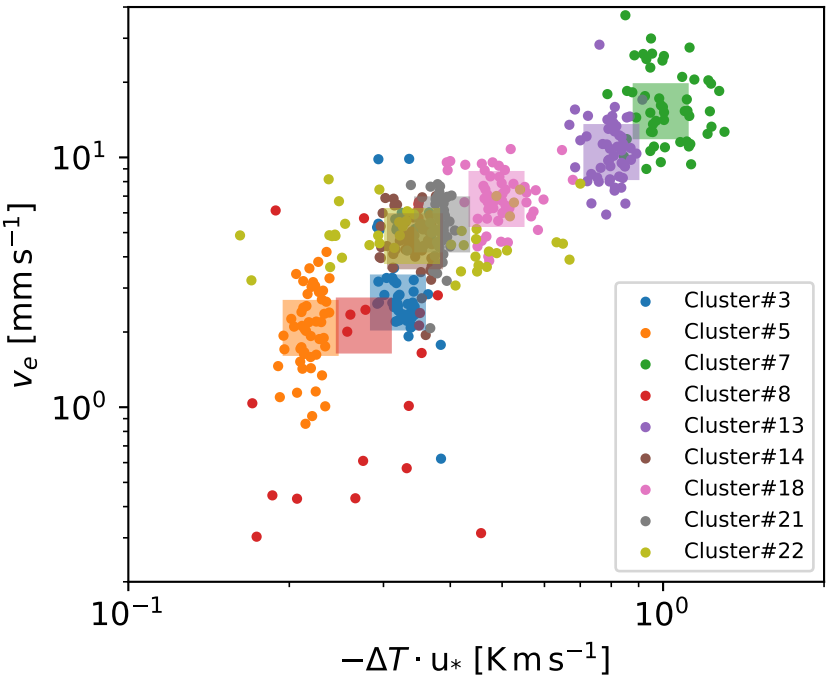

Figure S10. Entrainment rate v_e estimated from each cluster pair via Eq. (4) as function of $-\Delta T_{\text{Unstable}} \cdot u_*$. The small dots denote the results from the individual bootstrap runs and the squares the median values per cluster.

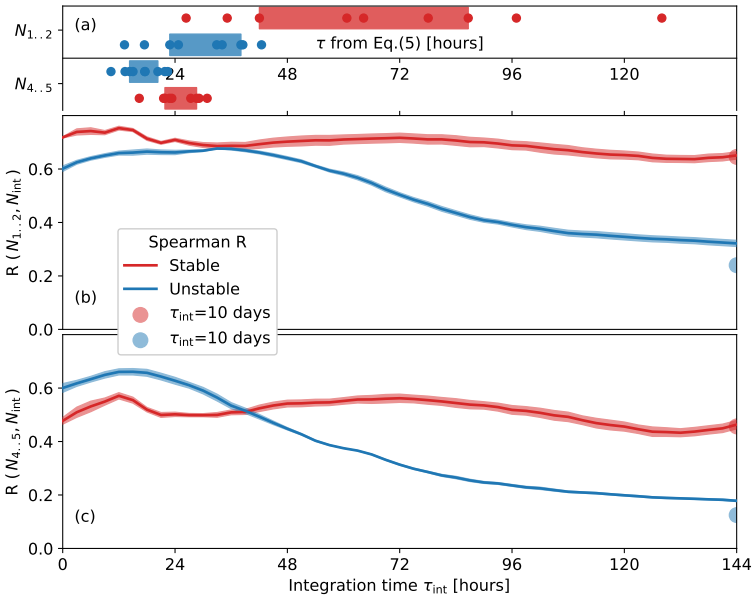

Figure S11. (a) $\tau_{1..2}$ and $\tau_{4..5}$ calculated form Eq. (5) for the cluster pairs. The shaded squares indicate the ranges; (b) Spearman rank coefficient between the observed number concentrations $N_{1..2}$ and $N_{1..2}$predicted(τ_{int}) as function of the integration time τ_{int} for stable and unstable atmospheric conditions. R reached for τ_{int}=10 days is indicated by the transparent markers; (c) same as (b) but for $N_{4..5}$.